Chapter 6: Ice Shedding from Wind Turbines

1. Introduction to Ice Shedding

Wind power is an excellent source of renewable energy in areas with sufficient wind resources. Usually, the best locations for wind turbines are on the tops of hills and ridges, where there are lower temperatures [1]. Cold temperatures are responsible for novel challenges [2, 3]. Due to cold climatic conditions, turbine blades are subjected to icing [4]. A number of methods have been proposed and tested for prevention and removal of ice on wind turbine blades, but no solution has been discovered to avoid it completely. The icing on the blades results in the phenomenon of 'ice shedding'.

Ice shedding is the loosening of ice from the blades. It has been reported that ice starts to loosen when its thickness reaches certain size [5]. This depends on weather conditions, turbine dimensions, rotational speed and other potential factors. This phenomenon is extremely dangerous for personnel and structures in the vicinity of the wind turbine. Icing happens on moving blades. When formed, it holds fast on the surface regardless of the inertia of the blade movement. It is reported that when the turbine is stopped and turned back on, a higher rate of ice shedding is observed. It is believed that this could be connected to a number of factors such (1) induced vibration due to the stoppage and (2) bending of the turbine blades (from deformed to undeformed positions) [6].

Wind turbines can accumulate ice under certain atmospheric conditions, such as ambient temperatures near freezing (0°C) combined with high relative humidity, freezing rain or sleet [7, 8]. The accumulation of ice is highly dependent on local weather conditions and the turbine's operational state [9]. There are many negative consequences of ice accretion on wind turbines. The icing of the blades can cause a complete loss of power production. According to the survey reported in [10], during 1998 to 2003, due to the low temperature one of the wind parks in Sweden stopped for maintenance 92 times out of a total 1337 times (lost 8022h out of 161523h energy). Most of the lost time (7353h, about 92%) was caused by ice accretion on blades [10]. The icing on the blades of the turbines can disrupt aerodynamics and lead to reduced power production. According to research [11] the increase in the roughness on the

blades' surface due to ice accretion may result in higher drag coefficient, resulting in reduced power production. Differences between the ice accretion on individual blades of a wind turbine cause imbalance in the rotor that can induce fatigue in the wind turbine assembly components. Sheets or fragments of ice to loosening and falling make the area directly under the rotor subject to significant safety risks. In addition, rotating turbine blades may propel ice fragments a distance from the turbine that may be up to several hundred meters. Falling ice may cause damage to structures and vehicles and can also cause injury to site personnel and the public unless adequate measures are put in place for protection. Figure 1 shows a piece of ice shed from a wind turbine in Nygårdsfjell wind park in Norway.

Figure 1: Piece of ice shed from a turbine in Nygårdsfjell wind park, Norway [12]

Figure 2(a) shows wind turbine blades under conditions of almost no wind. At the time of the photograph, the turbines were rotating but not generating any power. For comparison, a photograph of turbine producing power is shown in Figure 2(b). It can be noticed that wind turbine blade is bent. Wind turbine blade bends when producing power.

(a)

(b)

Figure 2: Wind turbine blades: (a) under no wind condition, (b) blades are moving and producing power [13]

It is known by the operators that stopping a wind turbine, which has ice build-up on the blades and then re-starting it often removes a lot of the ice. This could be due to the significant shift from the loaded blade (2 m deflection) to unloaded blade (zero deflection) and not due to the vibrations from stopping, which the operators thought was the cause [13].

It has been observed that there is an average deflection of about 2 ± 0.5 m due to the wind load. The variation of ± 0.5 m in the deflection is due to the gusts of the wind. An illustration of this observation is shown in Figure 3 [14].

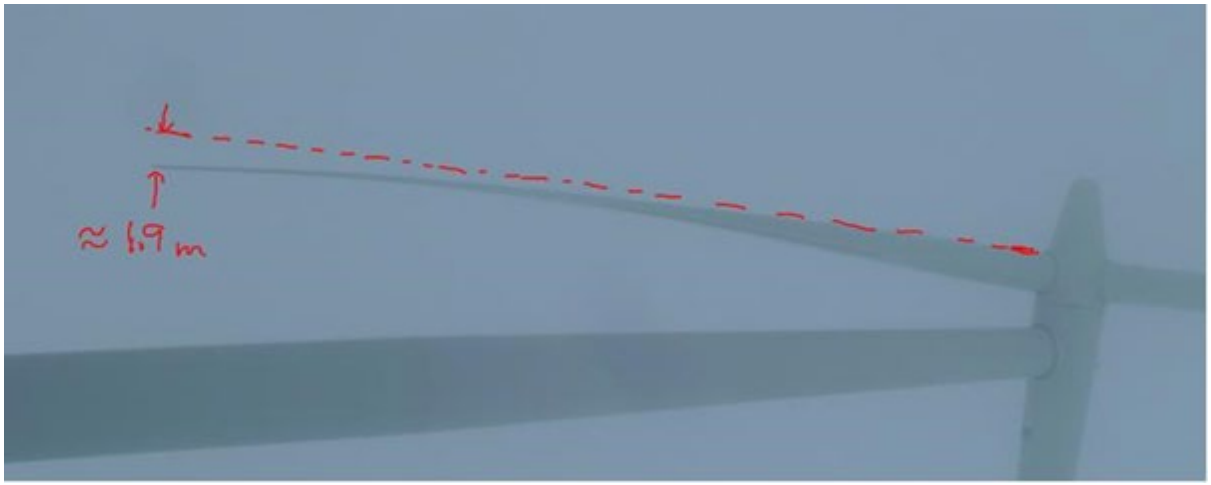

Figure 3: Demonstration of deflection in the wind turbine blade, the deflection at the tip of the blade is approximately 1.9 m [13].

2. Ice Formation

Ice forms due to the water droplets being cooled below the freezing temperature and pressure (0°C @ 1atm) and freeze and may adhere upon the impact with the structure . The key source of ice over wind turbine blades comes from the atmosphere [15]. To study the ice shedding, it is necessary to understand why icing takes place at first and what are possible remedial actions [16-19]. The atmospheric icing is defined as the accretion of ice or snow on structures that are exposed to the atmosphere [20-23]. In general, there are three sources of atmospheric icing such as In-cloud icing, Precipitation icing and Frost icing. In cloud and precipitation, icing creates ice that holds fast to the wind turbine and results in the phenomenon of ice shedding.

It happens when super-cooled water droplets hit a surface below 0℃ and freeze upon impact. The droplets temperature can be as low as -30 ℃ and they do not freeze in the air, because of their size. This type of ice accretion may have different sizes, shapes and properties, depending on the number of droplets in the air (liquid water content - LWC) and their size (median volume diameter - MVD), the temperature, the wind speed, the duration, the chord length of the blade and the collection efficiency.

There is a continuum of ice accretion appearance from rime at coldest temperatures to glaze at warmest.

The physical properties and the appearance of the accreted ice will vary widely according to the variation in meteorological conditions during the ice growth. [21, 23] give the typical properties of accreted atmospheric ice.

Table 1 Typical properties of accreted atmospheric ice [21, 23]

Type of ice	Density (kg/m^3)	Adhesion and cohesion	General appearance	
			Color	Shape
Glaze	900	Strong	transparent	evenly distributed/icicles
Wet snow	300 to 600	weak(forming) strong (Frozen)	white	evenly distributed/eccentric
Hard rime	600 to 900	strong	opaque	eccentric, pointing windward
Soft rime	200 to 600	Low to medium	white	eccentric, pointing windward

Rime is the most common form of in-cloud icing. It forms through deposition of super cooled fog or cloud droplets. During the icing event, different droplet size and air temperature can give the rime different density and strength, which leads to form two subtypes of rime – hard and soft. Hard rime is harder to move because the higher MVD and LWC cause accretion with higher density. Soft rime appears when the temperature is well below 0°C, and the MVD and LWC are small. It is formed as thin ice with needles and flakes. Soft rime has low density and little adhesion and hence can easily to be removed. Low temperatures and small droplet size typically lead to an ice accretion of low density and low strength.

The glaze is a smooth, transparent and homogeneous ice coating occurring when freezing rain or drizzle hits a surface [24]. Glaze has a high density and strong adhesion and is harder to remove than rime. It is often associated with the

precipitation. A sample of glaze ice is given in Figure 2 [14]. It is a result of ice shedding from a wind turbine blade.

Figure 4: Glaze ice from a wind turbine blade [14]

Precipitation ice can be snow or rain. The accretion rate can be much higher than in-cloud icing and hence could be more damaging [24]. Precipitation icing may result from two sources ‘wet snow’ and ‘freezing rain’. ‘Wet snow’ can adhere to a surface when it is liquid at air temperature between 0°C and 3°C. If the temperature is decreasing after wet snow accretion, the snow will freeze. It is due to the snow having some liquid water present, which allows the snow crystals to bind together when they come in contact with the surface. It is easy to remove at first, but can be difficult if it freezes on the surface [20]. When rain falls at temperatures below 0°C, it leads to ‘freezing rain’. It often occurs in connection with a temperature inversion where cold air is trapped near the ground beneath a layer of warmer air [23]. It can also occur in the case of a rapid temperature rise where an object still has a temperature below freezing even though the air temperature is above freezing. Ice density and adhesion are high when this phenomenon occurs.

Ice exists in a number of different crystal structures, as well as two amorphous states [25]. The ordinary ice we find in our freezer is hexagonal crystal structure that is called ice-Ih as shown in Figure 5. The numbers refer to individual water molecules [26].

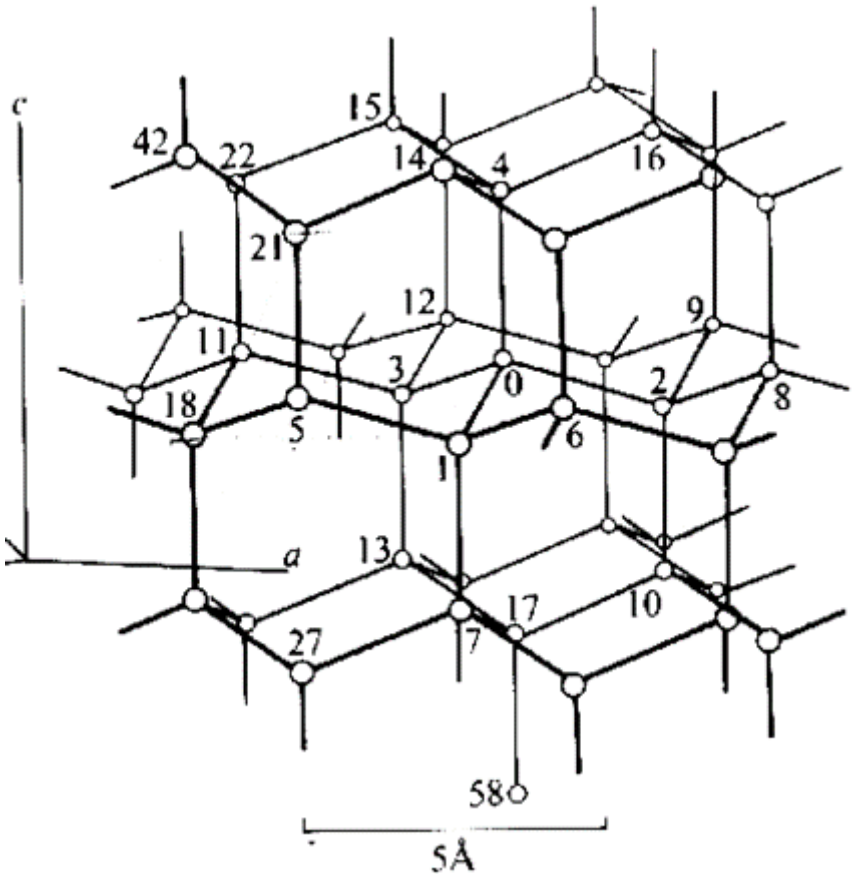

Figure 5: The structure of ice-Ih [25].

A common experience in handling pieces of ice tells us that ice is a brittle material. Therefore, the mechanical behavior of ice exhibits a similarity to the mechanical behavior of brittle ceramics [27].

The elastic modulus and Poisson's ratio of polycrystalline ice have been measured by subjecting plates of ice to biaxial bending [28]. At a temperature of −10°C for measurements on ice plates that were 0.5 m in diameter, the Young's modulus of ice was reported in the range of 4–9 GPa and Poisson's ratio was 0.29–0.32 [29]. Ice strength depends on the variables of temperature, strain rate, tested volume, and ice grain size.

The average tensile strength of ice from published investigations is 1.43 MPa in the temperature range −10°C to −20°C [30]. Over this temperature range, the compressive strength of ice ranges between 5–25 MPa [30]. Ice strength depends on the variables of temperature, strain rate, tested volume, and ice grain size.

It is known that the strength of ice increases with decreasing temperature in both tension and compression. As shown in Figure 6, the temperature effect on compression strength is more prominent than in tension strength, which is almost three times more during the temperature 0°C and −40°C [30].

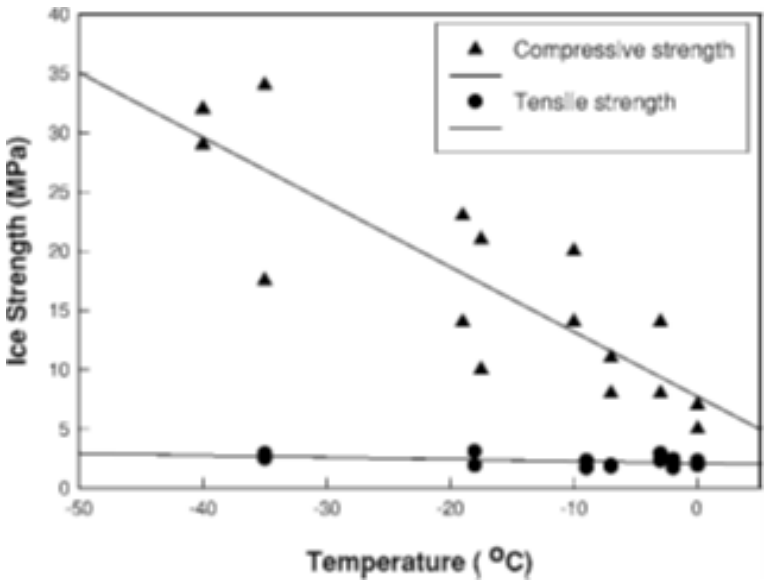

Figure 6: Tensile and compressive strength of ice as a function of temperature [30]

Schematic stress-strain curves. I, II, and III denote low, intermediate, and high-strain rates as shown in Figure 7. The arrows indicate either ductile (horizontal) or brittle (vertical) behavior. At low rates of deformation, cracks do not form, and the material is ductile (curves I). At high rates, cracks do initiate, and the material is brittle (curves III) and independent of the stress state. At intermediate strain rates, cracks also develop, and the material is brittle under tension (curve II-Tension) but ductile under compression (curve II-Compression). The ductile-brittle transition occurs at lower strain rates under tension because the applied stress opens the cracks directly. Under compression, the required tensile stress is generated locally through crack sliding. Note that the compressive stress-strain curve at intermediate strain rates displays a peak owing, we believe, to crack-induced localized flow [25].

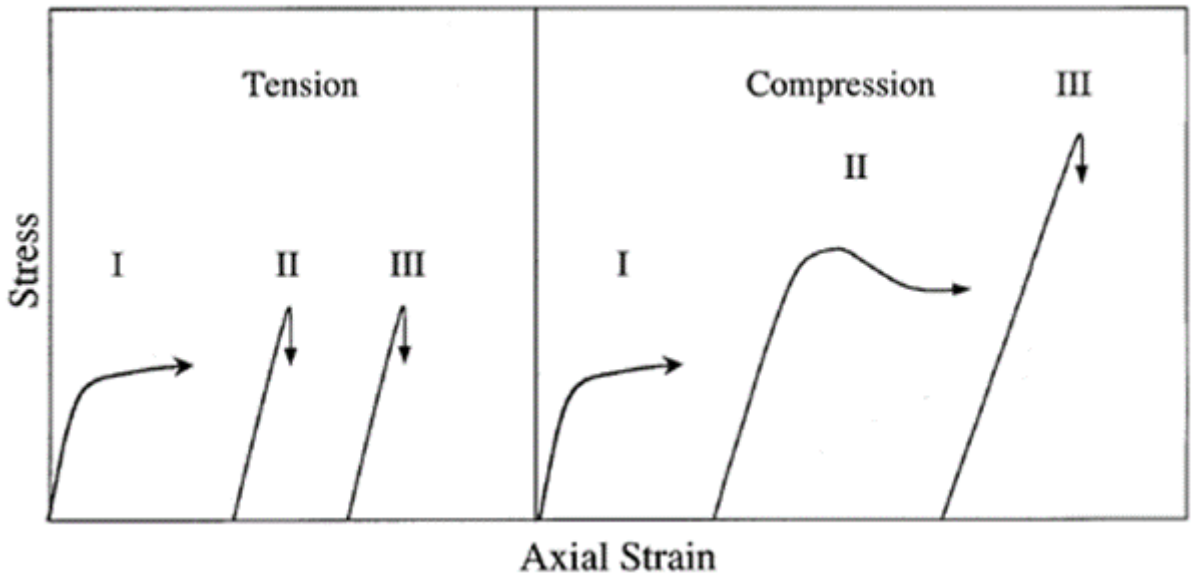

Figure 7: Schematic stress-strain curves [25]

The tensile and compressive strengths of fresh-water ice of about 1 mm grain size vs. strain rate are shown in Figure 8.

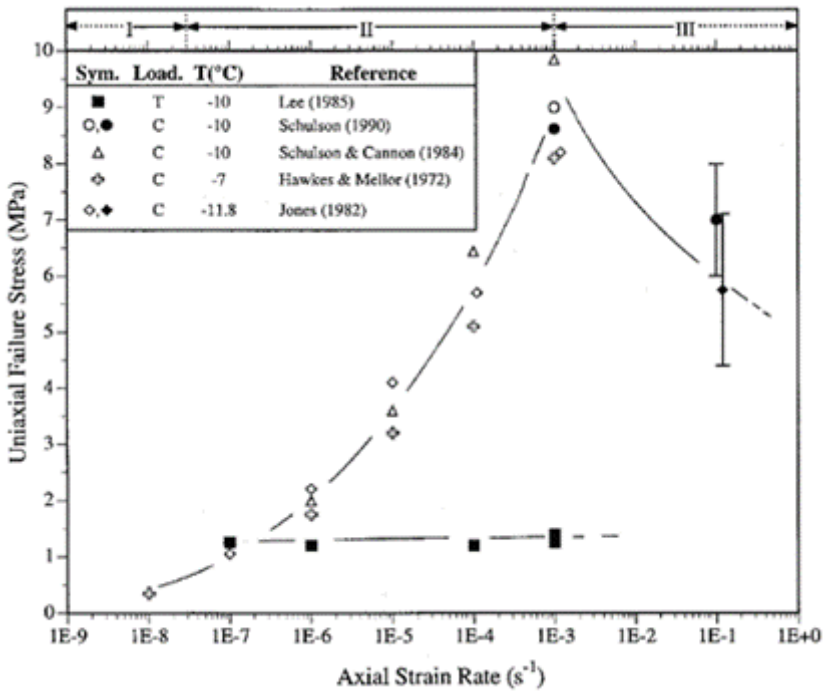

Figure 8: Tensile and compressive strengths of equiaxed and randomly oriented fresh-water ice of about 1 mm grain size vs. strain rate [31].

The tensile strength of ice decreases with the increase of grain size as shown in Figure 9. The given data of ice is recorded at a constant strain rate of $10^{-5} \cdot s^{-1}$ and temperature of -10°C.

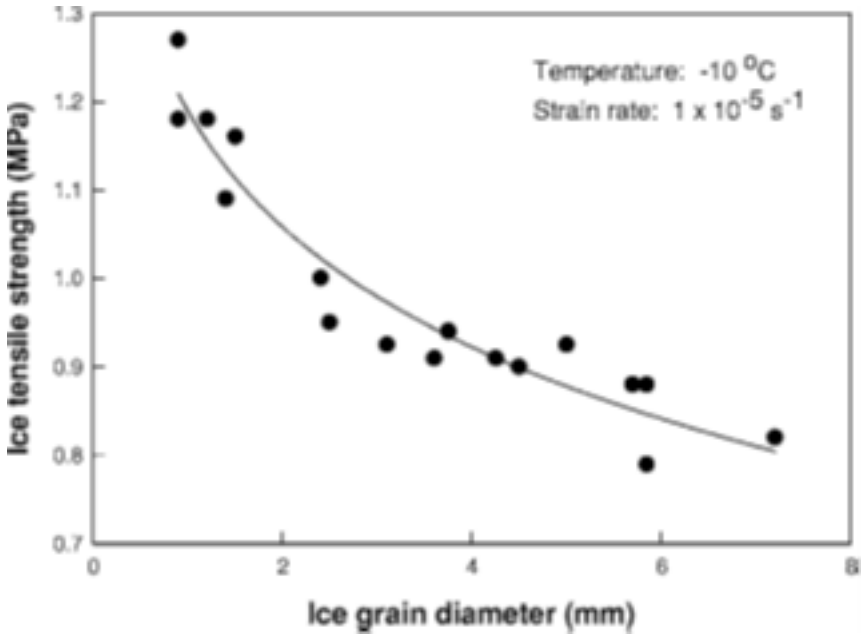

Figure 9: Tensile strength of ice as a function of grain size [31]

The tensile strength of ice decreases with increasing test specimen volume [32], as shown in Figure 10. Volume effects on the strength of brittle materials are usually described by a Weibull statistical distribution approach [33]. The Weibull theory is often referred to as a “weakest link” theory of fracture.

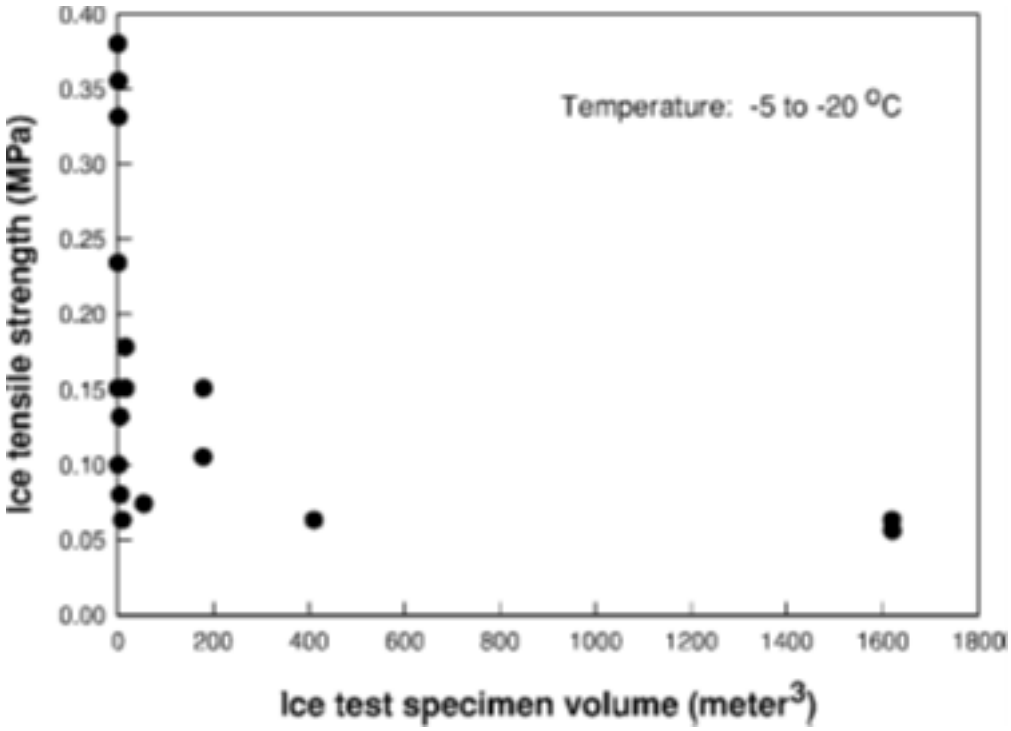

Figure 10: Tensile strength of ice with specimen volume [32]

There is no direct correlation to calculate the ice adhesion force [34]. However, researchers have given number theories [35, 36]. The theories divide the force of adhesion into four categories such as electrostatic adhesion, diffusive adhesion, mechanical adhesion and chemical adhesion. In electrostatic adhesion, the interface between the material and the ice adhere due to the transfer of electrical charges between them [37, 38]. In diffusive adhesion, material and ice adhere because the molecules at the surface diffuse across the interface into the matrix of the each other [39, 40]. In mechanical adhesion, material and ice adhere because water flows into the microscopic pores of the substrate and freeze, thereby, forming an interlocking mechanism of adhesion. As shown in Figure 11, a droplet of water in depression solidifies and expands, hence pushes apart the sides of the depression generating a grip [41]. Therefore, surface roughness has a significant effect on ice adhesion. For example, ice adhesion on the surface of stainless steel, in general, is up to 1.65 MPa, while the ice adhesion on the polished stainless steel is only 0.07 MPa [34].

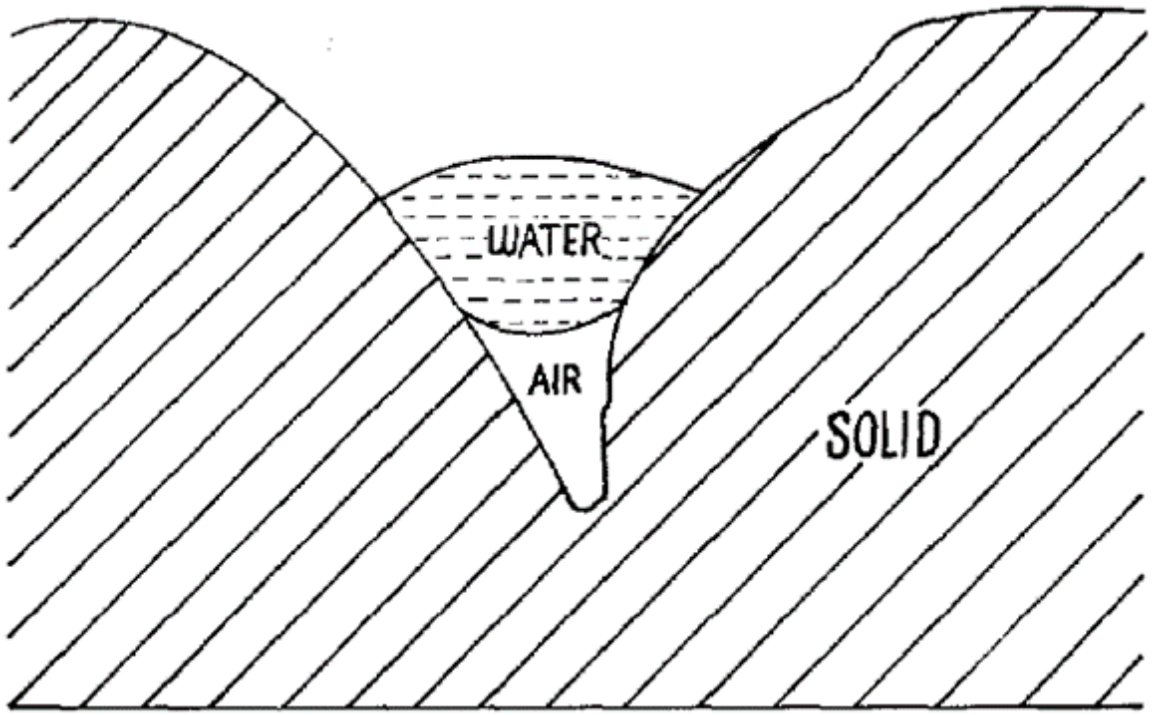

Figure 11: A water droplet in the micro-depression of solid surface [41]

In chemical adhesion, materials and the ice adhere because chemical bonds are formed between them at the interface. A number of different types of chemical bonds can be formed [42].

3. Multiphysics analysis of Ice Adhesion and Separation

In order to approach to the problem of the adhesion of ice, a two-layer laminate structure of ice and polymer material is designed. A four-point bending test is applied to investigate the separation of ice from a PVC surface [4, 43]. Different methods are used to analyse the results: theoretical, experimental and numerical simulations.

For the theoretical analysis the Euler-Bernoulli beam theory [44, 45] is solved in MATLAB®. For experimental work, ice is frozen over the PVC surface and loaded in a four-point bending test bench with a mounted strain gauge [46]. The numerical study is performed in ANSYS® Multiphysics by modelling the two materials: ice and PVC. The results from these studies reveal the longitudinal and shear stresses at the interface of the PVC surface and the ice separation behaviour.

3.1. Theoretical Analysis

The Euler-Bernoulli beam theory [44] can be used to calculate the maximum deflection in the centre of the four point bending specimen. Maximum deflection δ_{max} is given in Equation (1).

$$\delta_{max} = \delta_{center} = \frac{PL_1}{48EI_t}(3L^2 - 4L_1^2) \quad (1)$$

where δ_{center} is the deflection in the centre, L is the total length, L_1 is the distance between support point to loading point, E is Young's modulus and I is total moment of inertia about the neutral axis.

This specimen contains ice and PVC, two kinds of different materials, and therefore the rule of mixtures is introduced to find the material properties of the sample. It is valid to assume that under tensile loading, the Young's moduli of sample can be described as given in Equation (2).

$$E = E_{ice}\frac{A_{ice}}{A} + E_p\frac{A_p}{A} \quad (2)$$

where E, E_{ice} and $E_p$are Young's moduli of sample, ice and PVC respectively. A, A_{ice} and $A_p$are cross-sectional areas of sample, ice and PVC respectively.

Stress calculations in beams are performed with respect to the neutral axis. The neutral axis of a beam goes through the centroid of its cross section. Since there are two materials that have different young's moduli E_{ice} and E_p, it is safe to assume that $E_{ice} > E_p$, the expansion factor, also known as balance coefficient (n), is given in Equation (3).

$$n = \frac{E_p}{E_{ice}} \quad (3)$$

In order to have a similar inertial effect of both materials, the balance coefficient is multiplied by the width of PVC to create a hypothetical area. The neutral axis of the sample shifts because of the difference in the Young's moduli of ice and PVC, similarly, the values of the moment of area and the moment of Inertia also change. These values

are required to be calculated with respect to the new neutral axis (Equation (3)). The total moment of area Q_t and inertia I_t are given in Equations (4) and (5).

$$Q_t = Q_{ice} + Q_p \tag{4}$$

$$I_t = I_{ice} + I_p \tag{5}$$

where Q_{ice} is the area moment of ice, Q_p is area moment of PVC, I_{ice} is the moment of inertia of ice and I_p is the moment of inertia of PVC. Q_{ice} , Q_p , I_{ice} and I_p are given in Equations (6) to (9).

$$Q_{ice} = t_{ice} \cdot b \cdot (\overline{y}_{ice} - \overline{Y}) \tag{6}$$

$$Q_p = t_p \cdot n \cdot b \cdot (\overline{y}_p - \overline{Y}) \tag{7}$$

$$I_{ice} = \frac{b \cdot t_{ice}^3}{12} + b \cdot t_{ice} \cdot (\overline{y}_{ice} - \overline{Y})^2 \tag{8}$$

$$I_p = \frac{n \cdot b \cdot t_p^3}{12} + n \cdot b \cdot t_p \cdot (\overline{y}_p - \overline{Y})^2 \tag{9}$$

where $\overline{y}_{ice}$ and $\overline{y}_p$ are distances of the neutral axis of ice and PVC from the reference axis respectively.

The longitudinal stresses in the ice and PVC are given in Equations (10) and (11).

$$\sigma_{x,ice} = -\frac{M(y - \overline{Y})}{I_t} , \qquad (t_p \le y \le t_p + t_{ice}) \tag{10}$$

$$\sigma_{x,p} = -\frac{nM(y - \overline{Y})}{I_t} , \qquad (0 \le y \le t_p) \tag{11}$$

where $\sigma_{x,ice}$ and $\sigma_{x,p}$ are the longitudinal stresses in ice and PVC respectively. y is the position based on reference axis (placed at the bottom of the sample).

Similarly, shear stresses in the ice and PVC are given in Equations (12) and (13).

$$\tau_{x,ice} = \frac{VQ_{ice}}{I_t\, b} , \qquad (y = t_p) \tag{12}$$

$$\tau_{x,p} = \frac{nVQ_p}{I_t\, b}\,, \qquad (y = t_p) \tag{13}$$

where $\tau_{x,ice}$ and $\tau_{x,p}$ are the shear stresses at the interface of ice and PVC respectively.

3.2. Experimental Setup

The aim of the experiment is to generate observations of ice separation on a laboratory scale since bending induces longitudinal and shear stresses. Samples are prepared by freezing ice from tap water over the PVC surfaces (on the opposite side to the location of strain gauge) at -10℃ over 12 hours in the cold room test facility at UiT-The Arctic University of Norway (Narvik Campus). The length of the PVC plate is 260 mm, and all of this is covered with ice. The width and the thickness of the plate are 60mm and 1mm, respectively. The experiments are performed in the same conditions in order to avoid building any cracks in sample due to thermal shock. Thermal shock may introduce cracks in the ice samples and hence lead to erroneous results [47].

In order to investigate the separation of ice from a PVC surface, a four-point bending test bench is set up. Two different samples with ice thickness of 3 mm and 5 mm are investigated. In this setup the distance between the two supporting points is 200 mm and the distance from the supporting point to the loading point is 20 mm as shown in Figure 12.

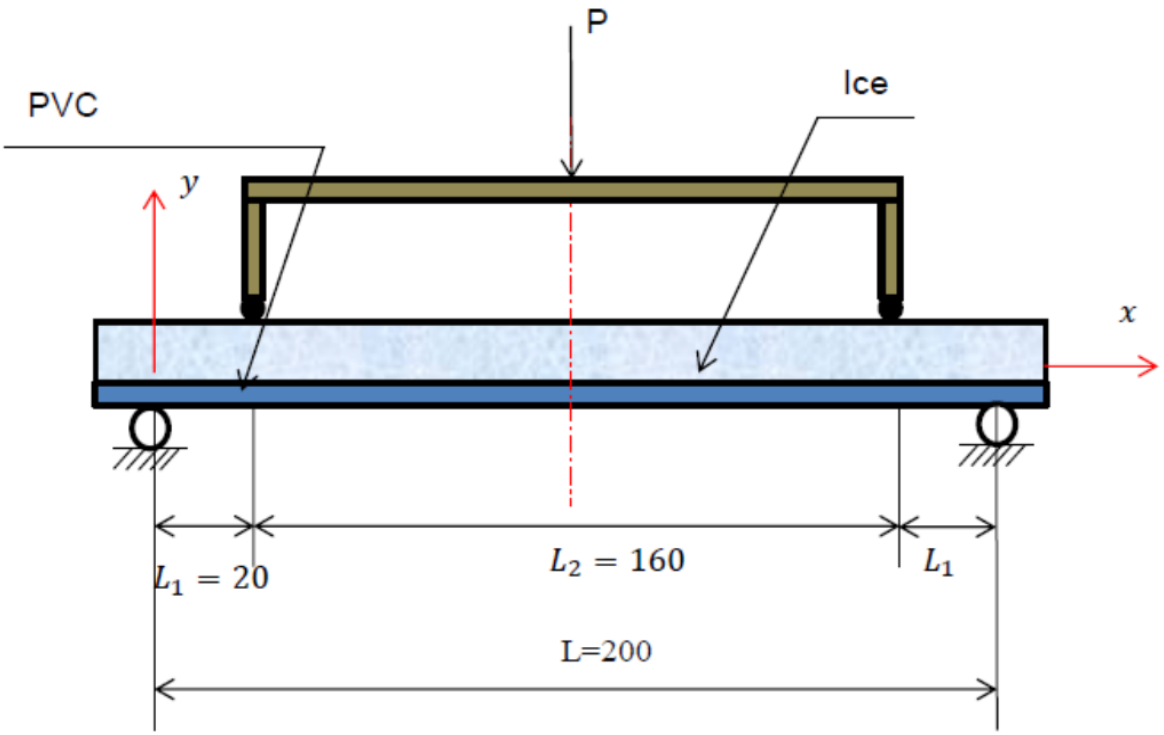

Figure 12: Four-point bending test setup of ice and PVC

In these experiments, loads are in the form of weights. These weights are placed gently by hand to produce strain in the sample. Deflections are recorded using a rosette strain gauge adhered to the bottom of a PVC sample as shown in Figure 13. The strain gauge is attached to a Wheatstone bridge circuit to give variation in voltage with the change in resistance. In this study, TML® FRA-5-23 strain gauges are used. These strain gauges have a gauge factor value of 2.15. The voltages are recorded using a data acquisition system. In this study a National Instrument® USB-6351 model, X Series Data Acquisition device is used to record strain. To connect the instrumental circuitry, various other cables, accessories, along with the data acquisition device are connected to a computer. The data is recorded in the National Instrument LabView® program. The data is recorded at 1 kHz over 1 sec for each load. It allows measuring of the strain more accurately since data can be averaged over time. Crude data (.lvm files) are processed in MS Excel to calibrate the results. The parameters are shown in Table 1.

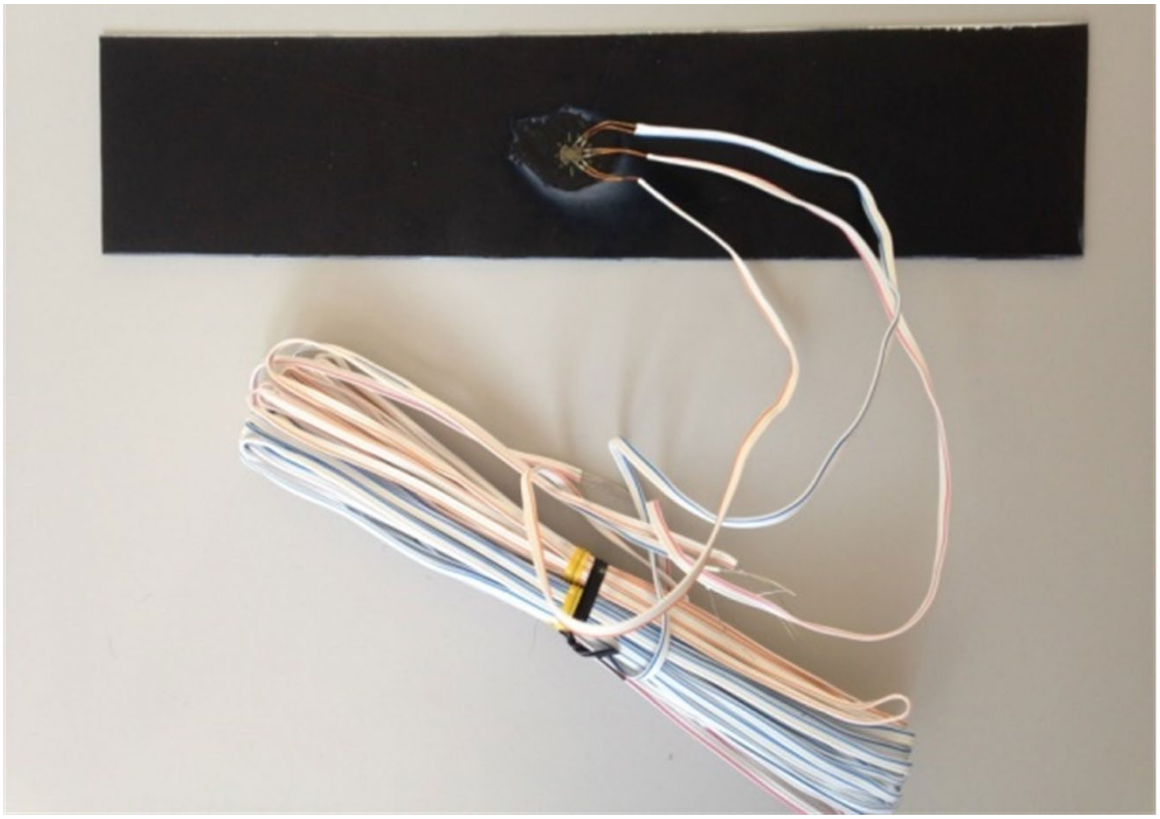

Figure 13: PVC surface of 260mm × 60mm × 1mm with a rosette strain gauge mounted in its geometric center.

Table 2: Description and values of parameters

Description	Variable	Units	value
Length of PVC and ice sample	l	mm	260
Width of PVC and ice sample	b	mm	60
Thickness of PVC	t_p	mm	1
Thickness of ice for sample 1	t_{ice}	mm	3
Thickness of ice for sample 2	t_{ice}	mm	5

Distance between the support and the load points	L_1	mm	20
Distance between the two load points	L_2	mm	160
Distance between the two support points	L	mm	200
Loads	P	g	varied

3.3. Numerical Simulations

The numerical studies are performed in ANSYS® Multiphysics. The geometric model is built and analyzed using numerical methods in ANSYS® Multiphysics, e.g., [48-59]. The dimensions of the geometric model are 260 mm long and 60 mm wide. The geometric model contains 12 volume segments. The volume segments provide the geometric features required to place the loading and boundary conditions on the model. The finite element (FE) model of ice and PVC sample is built using ANSYS® finite element (FE) brick 20 nodes solid 186 elements [60]. This element type provides more accurate results in comparison to solid 8 node brick 185 elements. However, the simulation run-time for solid 186 is considerably higher than solid 185 elements.

The FE models are tested for sensitivity by varying the element numbers as shown in Figure 14. Net displacement results for a node at a particular geometric location are used to test the sensitivity. Result for an FEM mesh of 31200 elements is considered as a reference. For other meshes, variations are calculated as given in Equation (14).

$$Fractional\ displacement\ results\ = \frac{Displacement_{Number\ of\ Elements}}{Displacement_{31200\ Elements}} \qquad (14)$$

Figure 14 is here

Figure 14: FEM meshes sensitivity analysis.

As shown in Figure 14 that FEM results are consistent with a number of elements equal to 7240, therefore it is valid to use an FEM model containing 10800 elements for further analysis. The displacement constraint is applied at the point of supports as shown in Figure 15. In FEM, the displacement constraints are applied in x and y directions. It is to be noted that the longitudinal axis is oriented in the z direction in this model. The forces are applied equally to the nodes as shown in Figure 16.

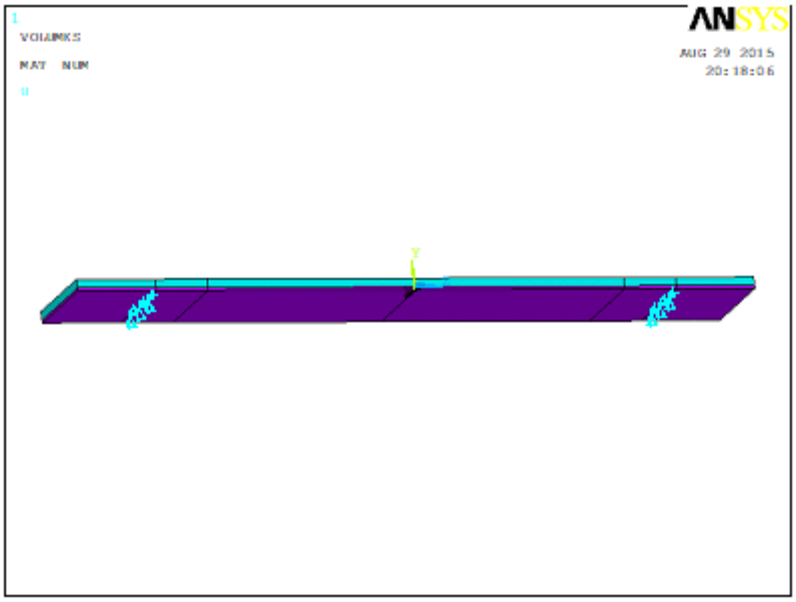

Figure 15: Applied displacements constraints on FEM model.

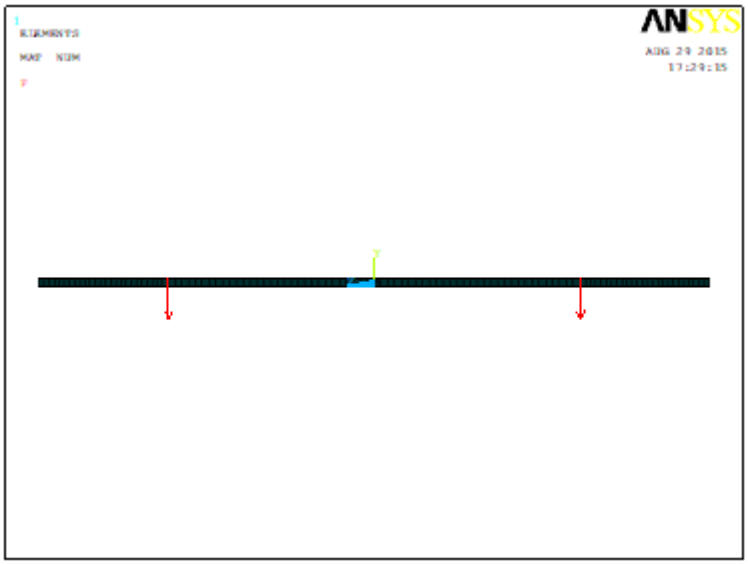

Figure 16: Applied forces on FEM model.

4. Results and Discussion

The results are given in three sections: theoretical, experimental and numerical simulation results. Theoretical results are obtained by solving Euler-Bernoulli beam theory for four-point bending in MATLAB®. Experimental results are achieved via strain gauge in four-point bending test bench. And numerical results are from linear static analysis in ANSYS® Multiphysics.

4.1. Theoretical Results

Three different results were obtained through theoretical analysis, i.e., maximum displacements in the samples with load, stress profile with a thickness of sample beam, stress profile in the longitudinal direction of the sample beam. The maximum displacement in the samples is calculated using the correlation of Equation (1) which is based on beam theory. To find the limits of theoretical results, the variation in gradient $\left(\frac{\delta_{max}}{P}\right)$ is tabulated as given in Table 3. It is shown that gradient values are more sensitive to the Young's modulus of ice in comparison to the Young's modulus of PVC.

Table 3: Gradient of maximum displacements with loads with variations in Young's moduli of ice and PVC

t_{ice} (mm)	Gradient ($\frac{mm}{g}$) E_{ice} = 4 GPa E_p = 1.5 MPa	Gradient ($\frac{mm}{g}$) E_{ice} = 9 GPa E_p = 1.5 MPa	Gradient ($\frac{mm}{g}$) E_{ice} = 4 GPa E_p = 15 MPa	Gradient ($\frac{mm}{g}$) E_{ice} = 9 GPa E_p = 15 MPa
3 mm	0.0012	5.31E-04	0.0012	5.29E-04
5 mm	2.32E-04	1.03E-04	2.31E-04	1.03E-04

The maximum displacements with loads for an ice Young's modulus of 4 GPa and a PVC Young's modulus of 15 MPa for a 5 mm thick ice sample are shown in Figure 17, which is produced using MATLAB® script.

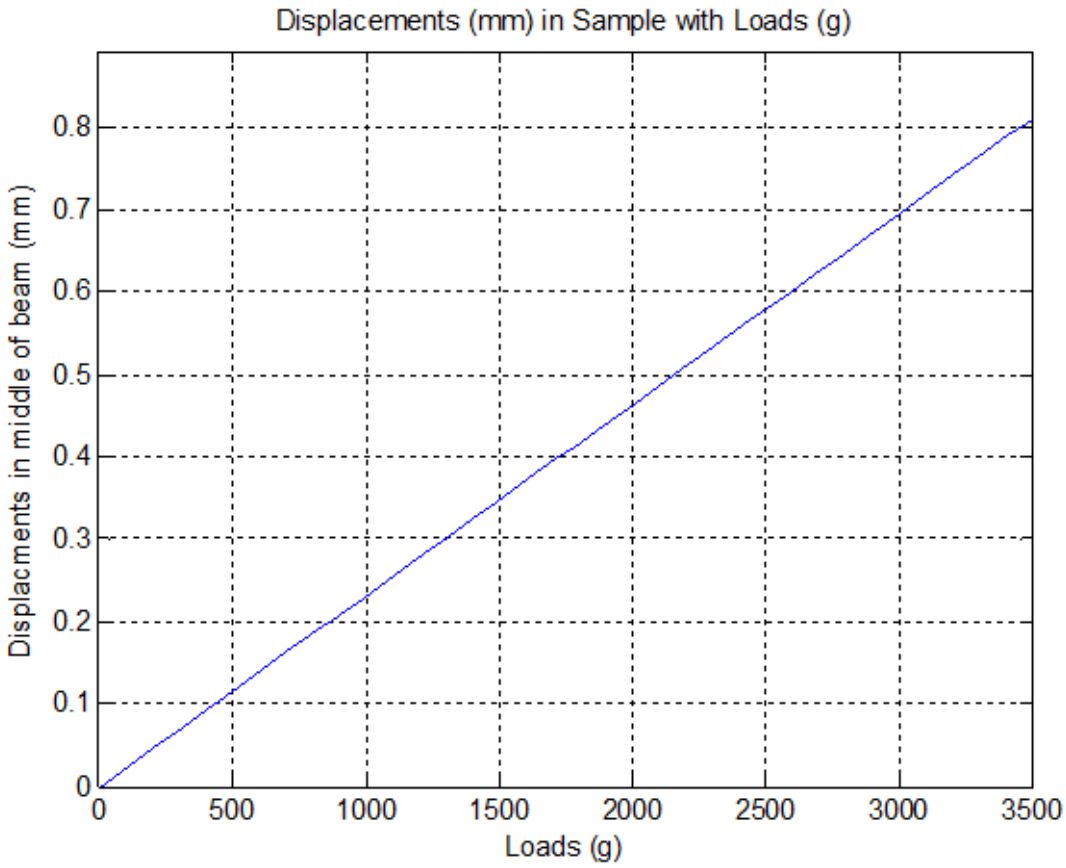

Figure 17: Displacements in middle of beam (mm) vs. loads (g) for an ice Young's modulus of 4 GPa and a PVC Young's modulus of 15 MPa for a 5 mm thick ice sample

The longitudinal stress is independent of the material property such as Young's modulus and directly proportional to the applied load. The maximum stress in the sample is limited by tensile strength. Stress more than the tensile strength will cause ice to fracture. The tensile strength of ice has been reported to be between 1 MPa to 1.5 MPa [31]. Loads responsible for this amount of stresses are given below: Maximum Longitudinal Stress across the thickness of a 3 mm ice sample under a load of 1000-1400 is 1.080-1.512MPa; Maximum Longitudinal Stress across the thickness of a 5 mm ice sample under a load of 2600-3900g is 1.016-1.523MPa. Figure 18 is shown the longitudinal stress across the thickness of a 5 mm ice sample under a load of 3900g.

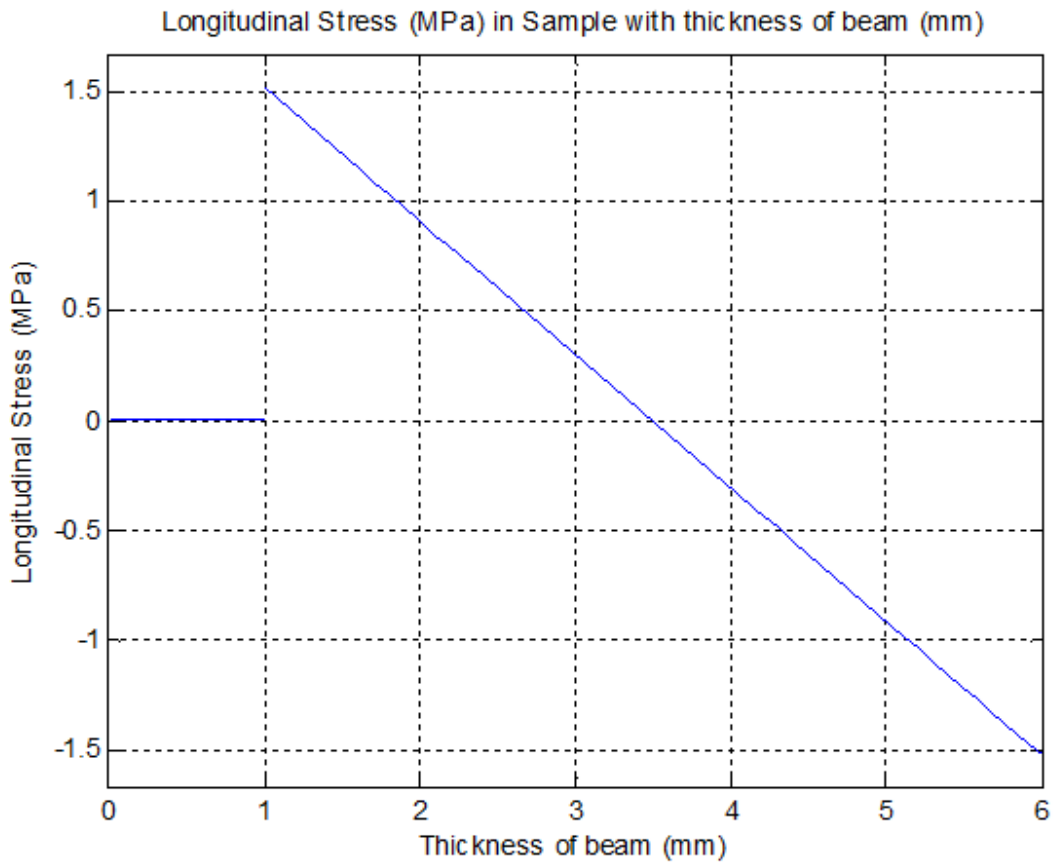

Figure 18: Longitudinal stress (MPa) along the thickness of sample for a 5 mm ice sample under the load of 3900g.

As shown, the tensile stress is maximum at the interface between ice and PVC and compressive stress is maximum at the top of the ice. There is negligible stress in PVC since it is softer than ice. The negative value of longitudinal stresses corresponds to compressive stresses. The longitudinal stress across the length of the sample for a 5 mm ice sample under a load of 3900 g is shown in Figure 19. It is shown that longitudinal stress is zero beyond the support point and varying linearly between the supports and loading points.

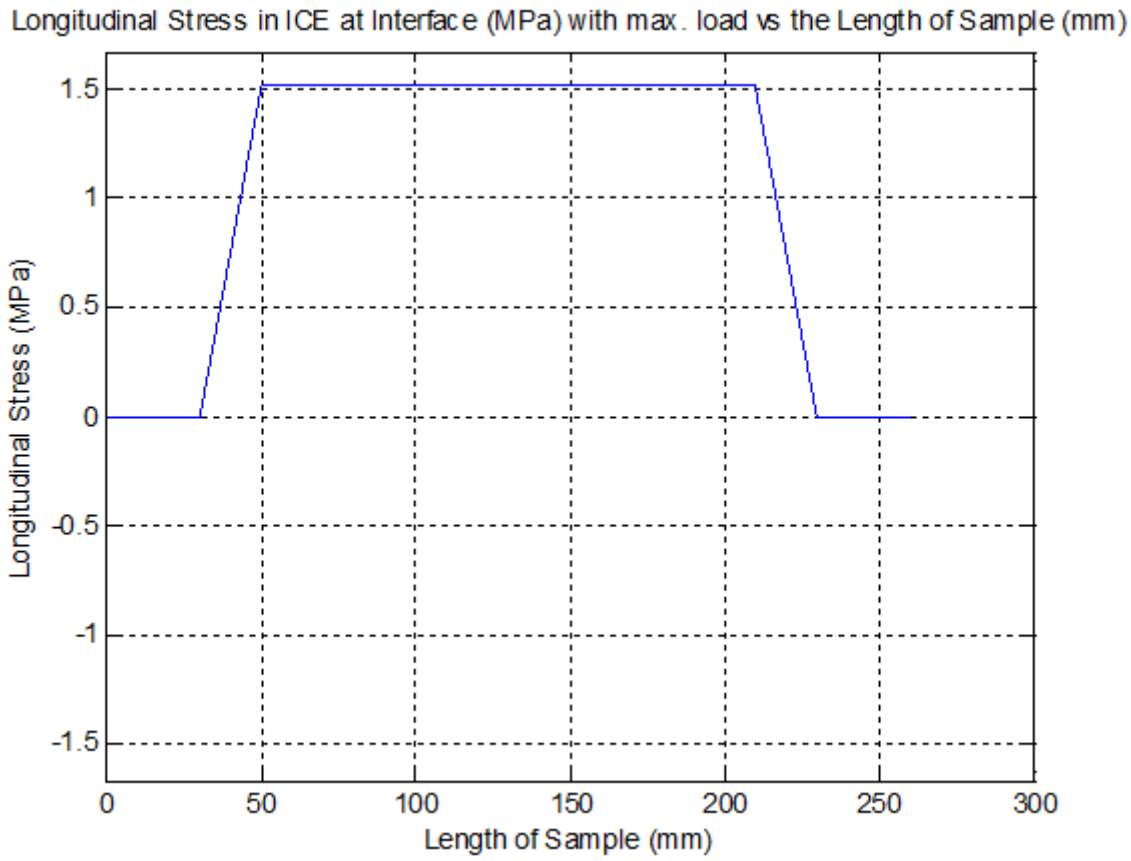

Figure 19: Longitudinal stress (MPa) along the sample length for a 5 mm ice sample under the load of 3900 g.

The shear stress is a function of material properties such as Young's modulus. The shear stress values of samples are shown with the Young's moduli of ice and PVC in Table 3. The shear stress causes the ice to separate from PVC. The adhesive strength of ice on a PVC surface is reported to be 234421 Pa (~34 psi) [41]. It is found that the shear stress experienced by the samples under maximum tensile loading is far less than this value. Therefore, it can be assumed that ice will undergo tensile failure prior to separation from a PVC surface. It is calculated that for a 3 mm thick ice sample that it will break and separate under a load of 1000-1400g and the maximum shear stress is 270-378 Pa, for a 5 mm thick ice sample, it will break and separate under a load of 2600-3900g and the maximum shear stress is 228-342 Pa.

Table 4: Shear stress with variations in Young's moduli of ice and PVC for a fixed load of 3500 g

t_{ice} (mm)	Shear Stress (Pa) E_{ice} = 4 GPa E_p = 1.5 MPa	Shear Stress (Pa) E_{ice} = 9 GPa E_p = 1.5 MPa	Shear Stress (Pa) E_{ice} = 4 GPa E_p = 15 MPa	Shear Stress (Pa) E_{ice} = 9 GPa E_p = 15 MPa
3 mm	95.2982	42.3737	946.1282	422.3767
5 mm	30.8891	13.7315	307.7777	137.0951

Variation in shear stress along the length of a 5 mm ice sample for an ice Young's modulus of 4 GPa and a PVC Young's modulus of 15 MPa under the load of 3900 g is given in Figure 20. It is to be noted that shear stress is zero beyond the support points and within the loading points and has a constant value between support and loading points. These results are in agreement with the four-point shear force diagram.

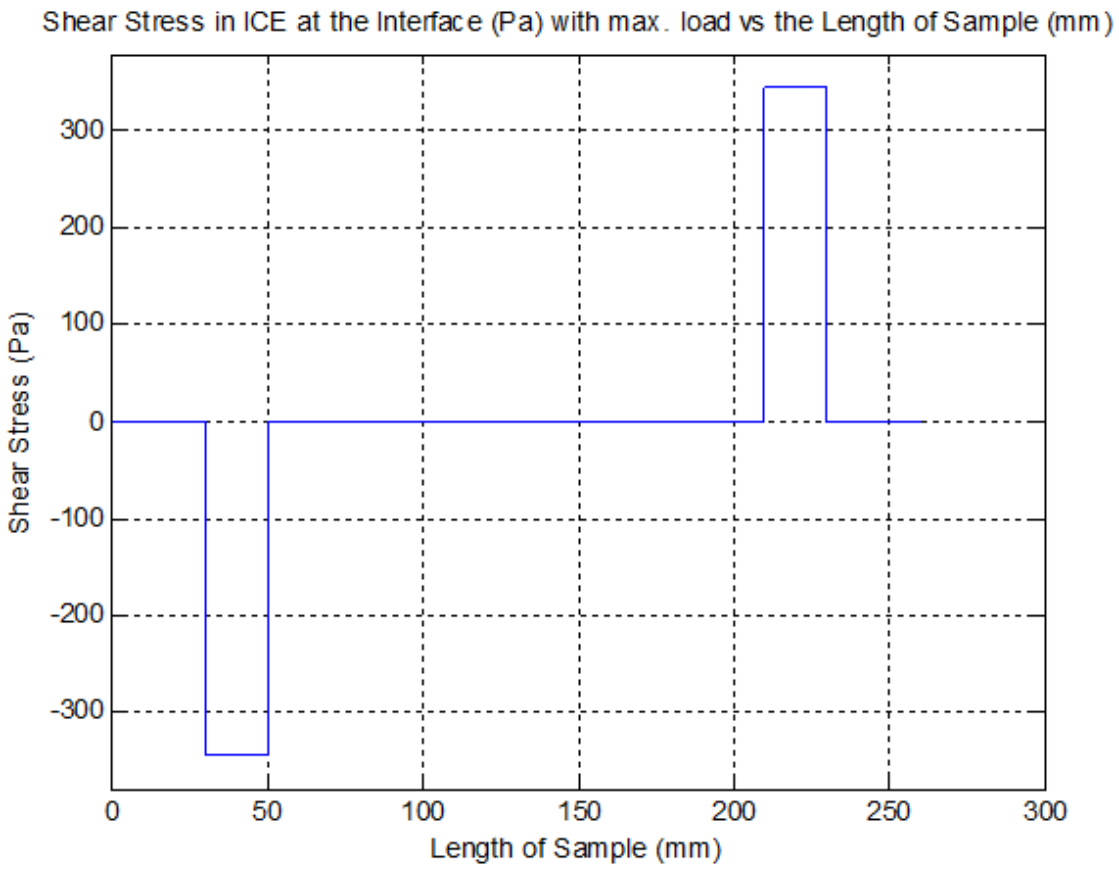

Figure 20: Variation in shear stress along the length of a 5 mm ice sample for an ice Young's modulus of 4 GPa and a PVC Young's modulus of 15 MPa under the load of 3900 g

4.2. Experimental Results

The replication of the mechanical behaviour of ice under flexural loading and the delamination of ice from the surface of PVC are the two key points to be noted. The experiments are repeated with both thicknesses 3 mm and 5 mm ice samples. The displacement with load for each sample is given in Figure 21 and Figure 22.

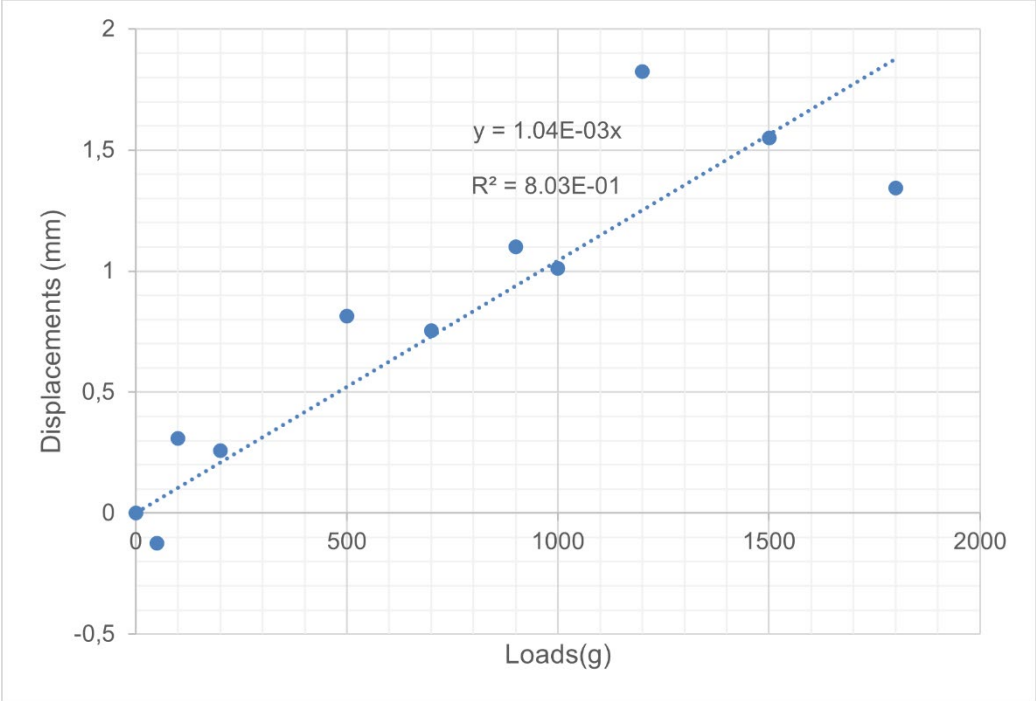

Figure 21: Displacement with variation in load for 3 mm thick ice sample

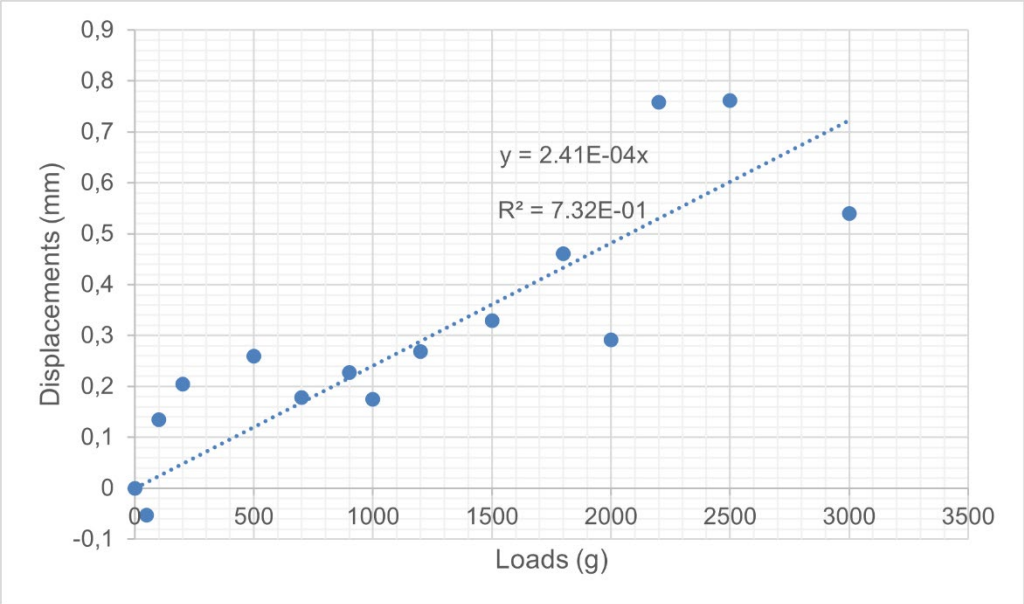

Figure 22: Displacement with variation in load for 5 mm thick ice sample

The experiments show that the gradient of displacement with load for 3 mm and 5 mm thickness ice samples are 1.04E-03 mm/g and 2.41E-04mm/g, r-squared value is

80.3 % and 73.3 % respectively. R-squared values indicate the fitness of data with the proposed linear equation. These values were used to calculate the Young's Modulus of ice using the procedure given before. The results were obtained for three different Young's Modulus for PVC: 1.5 MPa, 7 MPa and 15 MPa. In addition, r-squared value indicate that experimental results of 3 mm and 5 mm samples have a deviation of 19.7% and 26.8% respectively. The experimental results for the Young's modulus of ice are given in Table 5.

Table 5: Young's moduli of ice from the experimental results

Thickness of ice (mm)	Assumed PVC Young's Modulus (MPa)	Ice Young's Modulus from Experiments (GPa)	Deviation in results (GPa) based on R-squared value
3	1.5	4.70	+/- 0.93
	7	4.70	+/- 0.93
	15	4.70	+/- 0.93
5	1.5	3.85	+/- 1.03
	7	3.85	+/- 1.03
	15	3.85	+/- 1.03

It is found from the results that Young's moduli of ice do not vary with Young's moduli of PVC. Also, the obtained values of Young's modulus are in reasonable proximity to the values reported in the literature [28, 29, 61]. The deviation in the results is indicative of factors such as noise in strain gauges, handling of loads, instrumentation error, etc.

The maximum loads at the time of failure for 3mm and 5mm thickness of ice sample are 1800g and 3500g respectively. It is calculated that the corresponding longitudinal

stresses for 3mm and 5mm thickness of ice sample are 1.96 MPa and 1.37 MPa respectively, and shear stresses for each load are 41.7 Pa and 32.1Pa accordingly. It is found that maximum longitudinal stresses are in reasonable proximity of the reported values of the tensile strength of ice [31].

The failures in 3mm and 5mm ice samples are shown in Figure 23 and Figure 24.

Figure 23: Failure in 3 mm ice sample

As shown in Figure 23: Failure in 3 mm ice sample, that ice has gone through fractures, and a part of it is still in adhesion to the PVC surface.

Figure 24: Failure in a 5 mm ice sample

As shown in Figure 24, that ice has gone through fracture from various points and separated from the PVC surface. This is indicative of adhesive failure. Residuals of ice are noticeable on close observation of PVC surfaces. This is indicative of cohesive failure. It is obvious that shear stress from bending was not enough to overcome the adhesive strength of ice and PVC (reported to be 234421 Pa (~34 psi) [41]). The fracture had introduced localised stress concentration which had contributed to the crack propagation at the interface and hence lead to the separation of ice from the PVC surface [62].

4.3. Numerical Simulations Results

Numerical analysis was carried out in ANSYS® Multiphysics. Results of maximum displacement in samples with load and longitudinal stresses are obtained. Figure 25 shows displacement results from a 5 mm sample under a loading of 3500g. Numerical results of displacement gradient with load are 1.036E-03 mm/g and 2.409E-04 mm/g for 3 mm sample and 5 mm sample respectively.

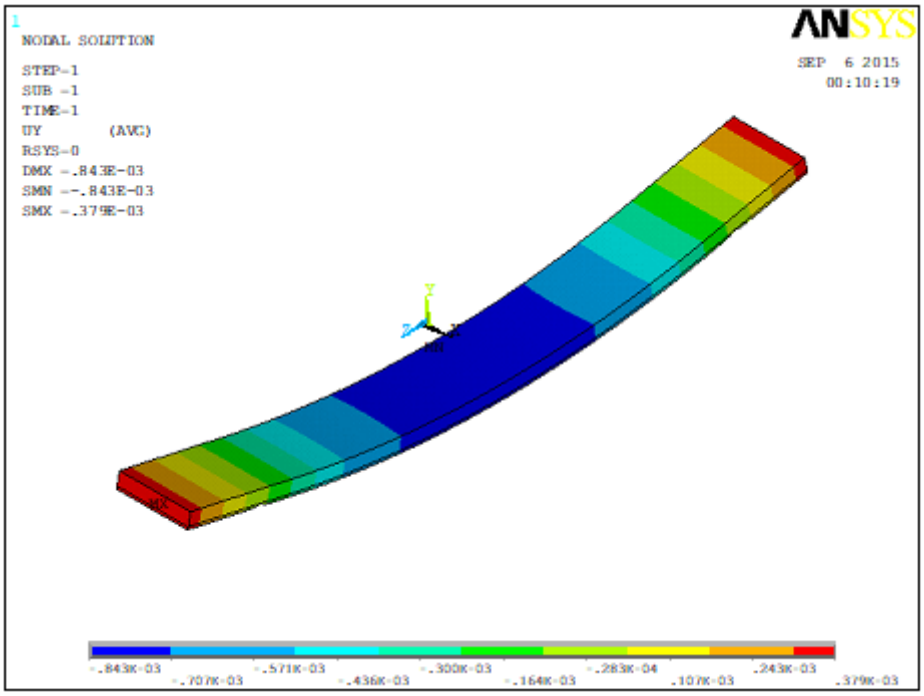

Figure 25: Displacement in the sample with 5 mm ice thickness loaded under 3500g.

The obtained longitudinal stress results for a 3 mm sample under a loading of 1800 g are shown in Figure 26 with a zoomed-in view shown in Figure 27.

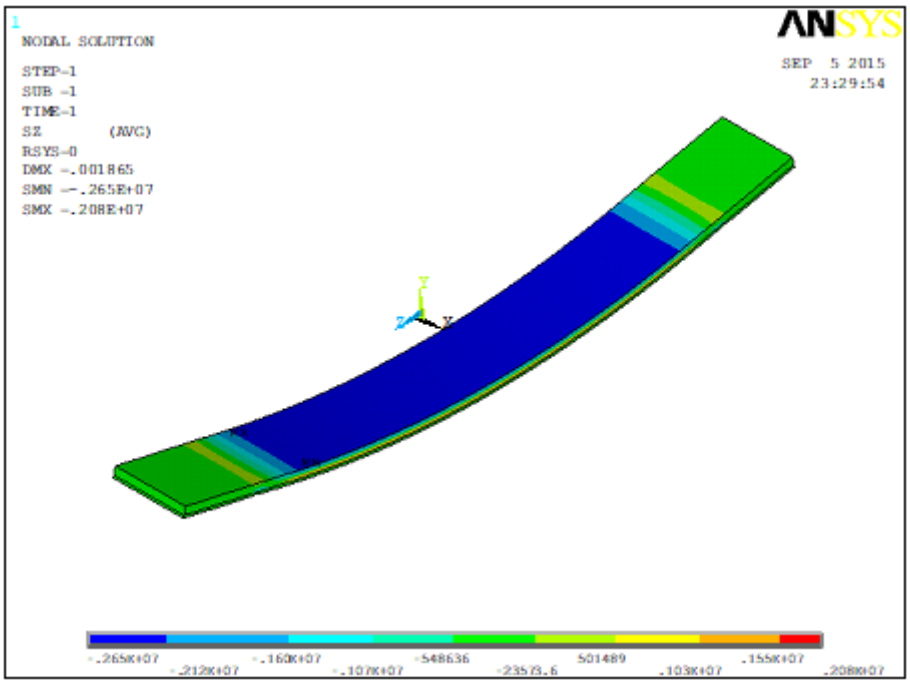

Figure 26: Longitudinal stress in the sample with 3 mm ice thickness loaded under 1800g.

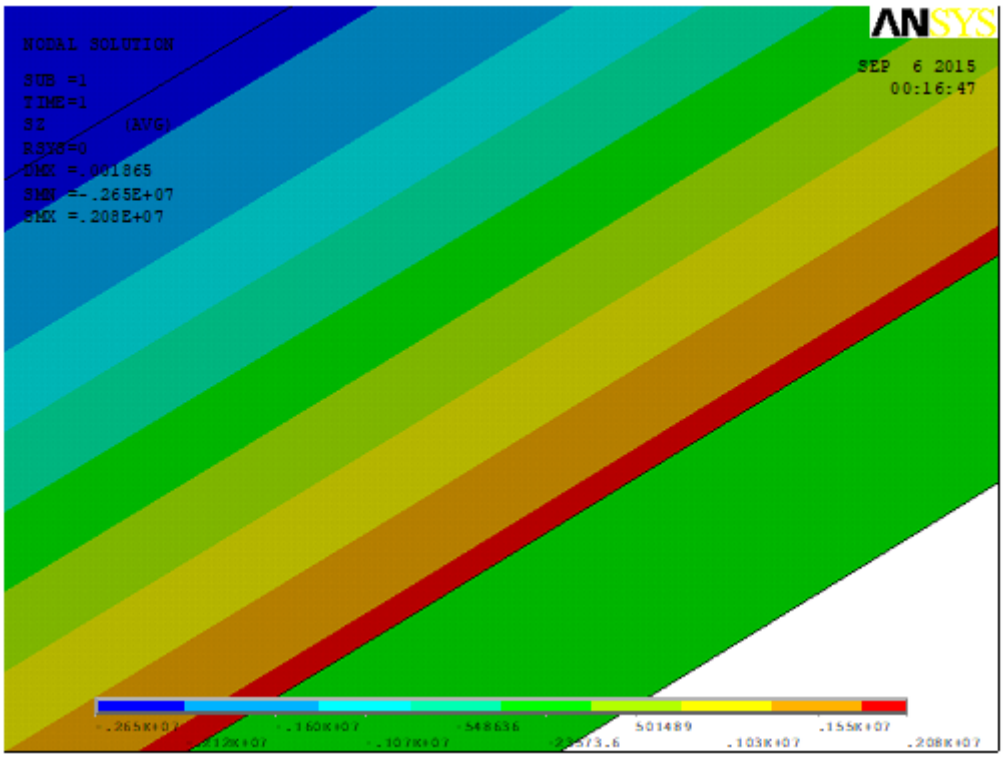

Figure 27: Zoomed-in view of longitudinal stress in the sample with 3 mm ice thickness loaded under 1800 g.

The obtained longitudinal stress results for a 5 mm sample under a loading of 3500 g are shown in Figure 28 with a zoomed-in view shown in Figure 29.

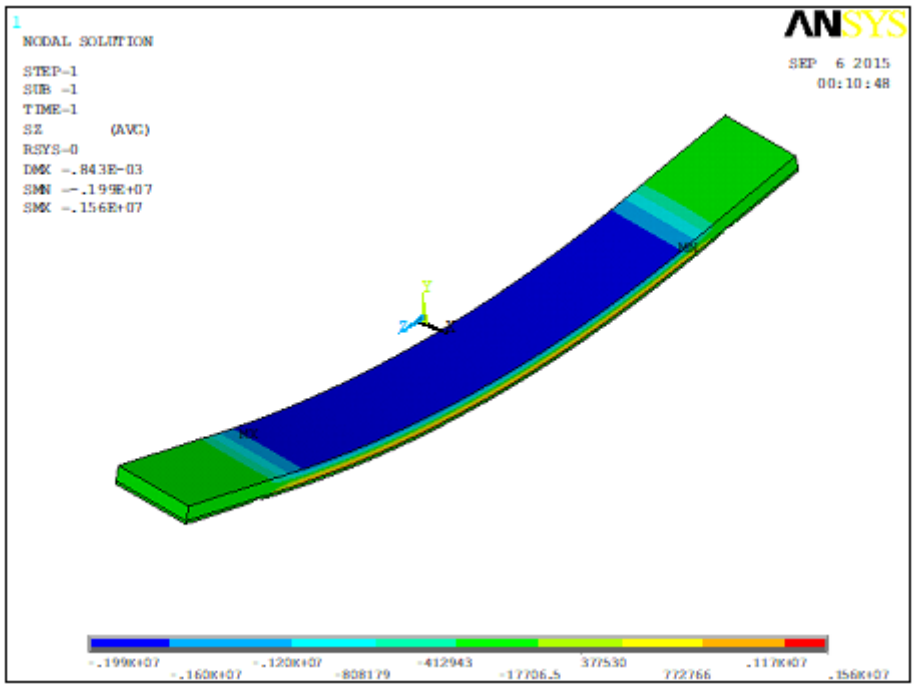

Figure 28: Longitudinal stress in the sample with 5 mm ice thickness loaded under 3500 g.

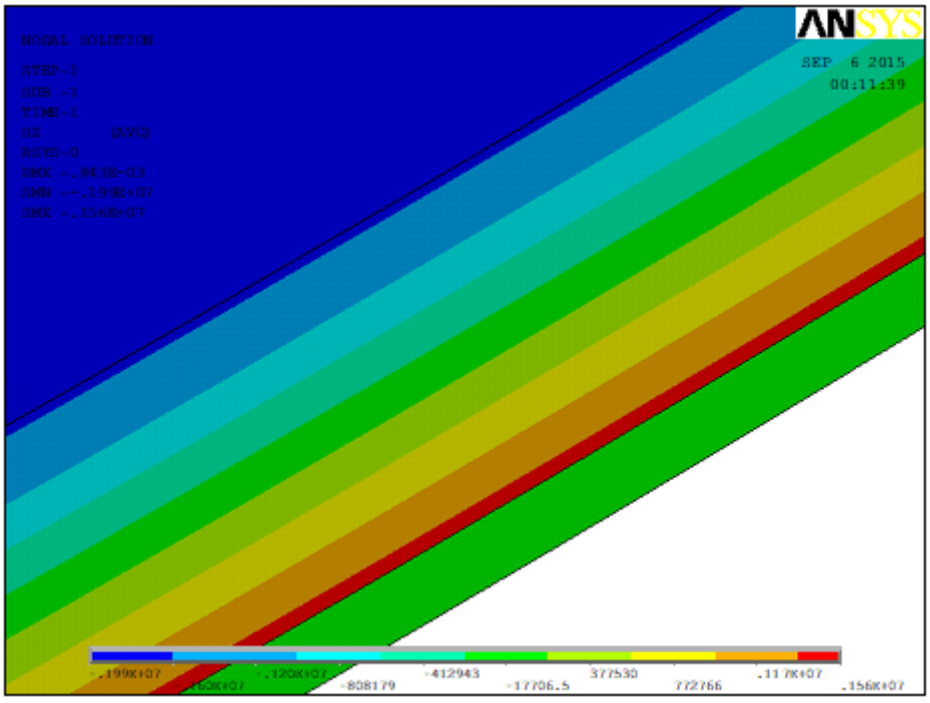

Figure 29: Zoomed-in view of longitudinal stress in the sample with 5 mm ice thickness loaded under 3500g.

The maximum tensile longitudinal stresses experienced by the samples are 2.08 MPa and 1.56 MPa for 3mm and 5mm thickness of ice sample respectively.

4.4. Comparison of Theoretical, Experimental and Simulation Results

It can be noted that values of displacement with load gradient and longitudinal stresses are in good agreement within different methodologies. Displacement with load gradients for various samples tested using theoretical, experimental and numerical analysis are presented in Table 6. Longitudinal stresses obtained through theoretical, experimental and numerical analysis are given in Table 7.

Table 6: Comparison of displacement with load gradients (mm/g)

(E_{ice} = 4 GPa and E_p = 15 MPa)

Ice thickness on 1 mm thick PVC sample	Theoretical analysis using rule of mixture and beam theory	Experimental results	Numerical results using FEM (ANSYS® Multiphysics)
3 mm	1.20E-03	1.04E-03	1.036E-03
5 mm	2.31E-04	2.41E-04	2.409E-04

Table 7: Comparison of longitudinal tensile stresses (MPa)

(E_{ice} = 4 GPa and E_p = 15 MPa)

Ice thickness on 1 mm thick PVC sample	Load at the time of failure (g)	Theoretical analysis using rule of mixture and beam theory	Experimental results	Numerical results using FEM (ANSYS® Multiphysics)
3 mm	1800	1.96	1.96	2.08
5 mm	3500	1.37	1.37	1.56

5. Conclusion

Ice shedding is a concerning phenomenon for wind turbine operations in cold regions. The phenomenon of ice shedding is of significant risk to personnel and equipment in nearby areas of wind turbines. The phenomenon of ice shedding is associated with mechanical failure of ice. This can be associated with bending in wind turbine blades since ice shedding is more prominent once iced turbine blades are stopped and turned back again. For building an understanding of the phenomenon of ice shedding, it is vital to understand the mechanical and adhesive properties of ice. A multiphysics analysis is presented to demonstrate the ice adhesion over an arbitrary material of PVC using theoretical analysis, experimental and numerical approaches. The theoretical study of this work is based on the use of the Euler-Bernoulli beam theory to solve a four-point bending problem to give the correlation of displacements with load, longitudinal stress and shear stress, and the rule of mixtures to derive common variables from two materials, such as Young's modulus, moment of inertia, and moment of area. Since adhesive forces can be categorized as either electrostatic, diffusion, mechanical and chemical as per the literature, there is no general correlation to work out the adhesive strength of ice over a particular surface except via experiments. Experiments with the help of theoretical analysis revealed the material properties of ice such as Young's modulus and tensile strength. The numerical analysis provided detailed results of displacement and longitudinal stresses in the two-material beam. A good agreement among theoretical, experimental and numerical

results confirms that ice can separate from a surface even when the shear force is not enough to overcome the adhesive strength. From the results it can be concluded that during the test the shear force is not enough to overcome the adhesive strength. Nonetheless, as fracture happens, the ice separates from the surface, which is associated with the crack propagation theory.

References

1. Ackermann, T. and L. Söder, *An overview of wind energy-status 2002.* Renewable and Sustainable Energy Reviews, 2002. **6**(1): p. 67-127.

2. Khawaja, H., D. Swart, and S. Antonsen, *Measuring environmental exposure*, in *https://www.ipo.gov.uk/p-ipsum/Case/PublicationNumber/GB2588580*, U.P. Office, Editor. 2019, Windtech: United Kingdom.

3. Ahmad, T., et al., *Study of Wind Chill Factor using Infrared Imaging.* The International Journal of Multiphysics, 2016. **10**(3): p. 325-342.

4. Xue, H. and H. Khawaja, *Review of the Phenomenon of Ice Shedding from Wind Turbine Blades.* The International Journal of Multiphysics, 2016. **10**(3): p. 265-276.

5. Scavuzzo, R. and M.L. Chu, *Structural properties of impact ices accreted on aircraft structures*. 1987: National Aeronautics and Space Administration.

6. Khawaja, H. and M. Moatamedi, *Selection of High Performance Alloy for Gas Turbine Blade Using Multiphysics Analysis.* The International Journal of Multiphysics, 2014. **8**(1): p. 91-100.

7. Rashid, T., H. Khawaja, and K. Edvardsen, *Determination of Thermal Properties of Fresh Water and Sea Water Ice using Multiphysics Analysis.* The International Journal of Multiphysics, 2016. **10**(3): p. 277-290.

8. Khawaja, H., et al., *Multiphysics Simulation of Infrared Signature of an Ice Cube.* The International Journal of Multiphysics, 2016. **10**(3): p. 291-302.

9. Morgan, C., E. Bossanyi, and H. Seifert. *Assessment of safety risks arising from wind turbine icing*. in *EWEC-CONFERENCE-*. 1997. BOOKSHOP FOR SCIENTIFIC PUBLICATIONS.

10. Ronsten, G., *Svenska erfarenheter av vindkraft i kallt klimat nedisning, iskast och avisning.* Elforsk rapport, 2004. **4**: p. 13.

11. Jasinski, W.J., et al., *Wind turbine performance under icing conditions.* Journal of Solar Energy Engineering, 1998. **120**(1): p. 60-65.

12. Homola, M.C., *Atmospheric icing on wind turbines.* Department of Technology, 2011: p. 152.

13. Xue, H., *Ice Shedding Processes*, in *Department of Engineering Design*. 2015, UiT-The Arctic University of Norway.

14. Homola, M., *Impacts and Causes of Icing on Wind Turbines*. 2005, Narvik University College.

15. Wahl, D. and P. Giguere, *Ice Shedding and Ice Throw–Risk and Mitigation.* General Electric Wind Application Engineering Group of GE Energy, 2006.

16. Dhar, S. and H.A. Khawaja, *Recognizing potential of LiDAR for comprehensive measurement of sea spray flux for improving the prediction of marine icing in cold conditions - A review.* Ocean Engineering, 2021. **223**: p. 108668.

17. Rashid, T., et al., *Roll to roll coating of carbon nanotube films for electro thermal heating.* Cold Regions Science and Technology, 2021. **182**: p. 103210.

18. Rashid, T., H.A. Khawaja, and K. Edvardsen, *Measuring thickness of marine ice using IR thermography.* Cold Regions Science and Technology, 2019. **158**: p. 221-229.

19. Rashid, T., H.A. Khawaja, and K. Edvardsen, *Review of marine icing and anti-/de-icing systems.* Journal of Marine Engineering & Technology, 2016. **15**(2): p. 79-87.

20. Boluk, Y., *Adhesion of freezing precipitates to aircraft surfaces.* 1996.

21. Fikke, S., et al., *Cost 727: atmospheric icing on structures.* Measurements and data collection on icing: State of the Art, Publication of MeteoSwiss, 2006. **75**(110): p. 1422-1381.

22. Richert, F., *Is Rotorcraft icing knowledge transferable to wind turbines.* BOREAS III. FMI, Saariselkä, Finland, 1996: p. 366-380.

23. 12494, I., *Atmospheric icing of structures*. 2001.

24. Oblack, R. *Glaze Ice definition*. 2015 [cited 2015 26-08-2015].

25. Schulson, E.M., *The structure and mechanical behavior of ice.* JOM, 1999. **51**(2): p. 21-27.

26. Hobbs, P.V., *Ice Physics*. 2010: OUP Oxford.

27. Schulson, E.M., *Brittle failure of ice.* Engineering Fracture Mechanics, 2001. **68**(17–18): p. 1839-1887.

28. Gold, L.W., *On the elasticity of ice plates.* Canadian journal of civil engineering, 1988. **15**(6): p. 1080-1084.

29. Voitkovskii, K., *The mechanical properties of ice*. 1962, DTIC Document.

30. Haynes, F.D., *Effect of temperature on the strength of snow-ice*. 1978, DTIC Document.

31. Currier, J. and E. Schulson, *The tensile strength of ice as a function of grain size.* Acta Metallurgica, 1982. **30**(8): p. 1511-1514.

32. Dempsey, J., et al., *Scale effects on the in-situ tensile strength and fracture of ice. Part I: Large grained freshwater ice at Spray Lakes Reservoir, Alberta*, in *Fracture Scaling*. 1999, Springer. p. 325-345.

33. Weibull, W., *A statistical theory of the strength of materials*. 1939: Generalstabens litografiska anstalts förlag.

34. Kulinich, S. and M. Farzaneh, *Ice adhesion on super-hydrophobic surfaces.* Applied Surface Science, 2009. **255**(18): p. 8153-8157.

35. Landy, M. and A. Freiberger, *Studies of ice adhesion: I. Adhesion of ice to plastics.* Journal of colloid and interface science, 1967. **25**(2): p. 231-244.

36. Houwink, R. and G. Salomon, *Adhesion and adhesives, Vol. 1*. 1965, Elsevier, New York.

37. Seidler, P., *New theories of adhesion of high polymers.* Adhaesion, 1963. **7**: p. 503-512.

38. Krotova, N., et al., *Investigation of various types of adhesion bonds*. 1965, DTIC Document.

39. Voiutskii, S.S., *Autohesion and adhesion of high polymers.* 1963.

40. Wake, W., *Theories of adhesion and uses of adhesives: a review.* Polymer, 1978. **19**(3): p. 291-308.

41. Bikerman, J.J., *The science of adhesive joints*. 2013: Elsevier.

42. *Adhesion Science and Engineering: Surfaces, Chemistry and Applications*. 2002: Elsevier Science.

43. Xue, H. and H. Khawaja, *Investigation of Ice-PVC separation under Flexural Loading using FEM Analysis.* The International Journal of Multiphysics, 2016. **10**(3): p. 247-264.

44. Bauchau, O.A. and J.I. Craig, *Structural Analysis: With Applications to Aerospace Structures*. 2009: Springer Netherlands.

45. Xue, H. and H. Khawaja, *Analytical study of sandwich structures using Euler–Bernoulli beam equation.* AIP Conference Proceedings, 2017. **1798**(1): p. 020076.

46. Andleeb, Z., et al., *Thermoelastic Investigation of Carbon-Fiber-Reinforced Composites Using a Drop-Weight Impact Test.* Applied Sciences, 2021. **11**(1): p. 207.

47. Lu, T. and N. Fleck, *The thermal shock resistance of solids.* Acta Materialia, 1998. **46**(13): p. 4755-4768.

48. Andleeb, Z., et al., *Strain Wave Analysis in Carbon-Fiber-Reinforced Composites subjected to Drop Weight Impact Test using ANSYS®.* The International Journal of Multiphysics, 2021. **15**(3): p. 275-290.

49. Brunner, D., et al., *CFD modelling of pressure and shear rate in torsionally vibrating structures using ANSYS CFX and COMSOL Multiphysics.* The International Journal of Multiphysics, 2018. **12**(4): p. 349-358.

50. Ludvigsen, S., et al., *Multiphysics Analysis of Contact Pressure Profile of Airless tires as compared to Conventional Tires.* The International Journal of Multiphysics, 2020. **14**(4): p. 399-425.

51. Andleeb, Z., et al., *Multiphysics Analysis of CFRP Charpy Tests by varying Temperatures.* The International Journal of Multiphysics, 2020. **14**(2): p. 143-160.

52. Stange, E., et al., *Multiphysics Study of Tensile Testing using Infrared thermography.* The International Journal of Multiphysics, 2019. **13**(2): p. 191-202.

53. Myrli, O. and H. Khawaja, *Fluid-Structure Interaction (FSI) Modelling of Aquaculture Net Cage.* The International Journal of Multiphysics, 2019. **13**(1): p. 97-112.

54. Myrvang, T. and H. Khawaja, *Validation of air ventilation in tunnels, using experiments and computational fluid dynamics.* The International Journal of Multiphysics, 2018. **12**(3): p. 295-312.

55. Khawaja, H., *Application of a 2-D approximation technique for solving stress analyses problem in FEM.* The International Journal of Multiphysics, 2015. **9**(4): p. 317-324.

56. Mughal, U., H. Khawaja, and M. Moatamedi, *Finite element analysis of human femur bone.* The International Journal of Multiphysics, 2015. **9**(2): p. 101-108.

57. Khawaja, H.A., et al., *Study of CRFP Shell Structures under Dynamic Loading in Shock Tube Setup.* Journal of Structures, 2014. **2014**: p. 487809.

58. Khawaja, H. and K. Parvez, *Validation of normal and frictional contact models of spherical bodies by FEM analysis.* The International Journal of Multiphysics, 2010. **4**(2): p. 175-185.

59. Khawaja, H., et al., *Optimization of elstomeric micro-fluidic valve dimensions using non-linear finite element methods.* The International Journal of Multiphysics, 2009. **3**(2): p. 187-200.

60. ANSYS®, *Academic Research, Theory Reference*, in *Mechanical APDL Guide*. release 14.0.

61. Nimmo, F. *What is the Young's Modulus of Ice?* in *Workshop on Europa's Icy Shell: Past, Present, and Future*. 2004.

62. Sih, G.C., *A special theory of crack propagation*, in *Mechanics of Fracture Initiation and Propagation*. 1991, Springer Netherlands. p. 1-22.